J. Mater. Chem. A, 2018, , 7133

Han Zhang,[a] Zongbin Zhao, *[a] Ya-Nan Hou,[a] Yongchao Tang,[a] Yanfeng Dong,[b] Shuang Wang,[a] Xiaojing Hu,[a] Zhichao Zhang,[c] Xuzhen Wang [ac] and Jieshan Qiu *[a]

Benefiting from the high theoretical specific capacity and low cost consumption, lithium–sulfur batteries have been regarded as the promising next-generation energy storage technology. However, lithium–sulfur batteries still encounter a series of challenges such as low conductivity and serious volumetric expansion of sulfur during the discharge process as well as the stubborn "shuttle effect" of polysulfides. Such problems have greatly plagued the real applications of lithium–sulfur batteries. Herein, we have synthesized below-5-nm g-C_3N_4 nanodots based on a pore confinement effect, and they are embedded in a MOF-derived N, S co-doped hollow porous carbon shell (CN@NSHPC) *via* a unique double solvent-induced strategy. CN@NSHPC displays superior lithium polysulfide (LiPS) adsorptivity and a high sulfur loading of 73%. When applied as an electrode in lithium–sulfur batteries, the CN@NSHPC electrode delivers an excellent specific capacity of 1447 mA h g^{-1} at 0.2C, good rate capability of 387 mA h g^{-1} at 5C, and excellent cycling stability, specifically, only 0.048% decay per cycle at 1.0C over 500 cycles. This proposed strategy provides an insight into a new pathway to construct co-doped carbon hollow nanostructure and nanodot materials by the pore confinement effect.

Received 17th January 2018
Accepted 19th March 2018

DOI: 10.1039/c8ta00529j

Lithium–sulfur (Li–S) batteries have been regarded as one of the most wonderful prospect for energy storage technologies. Compared with the current advanced lithium-ion batteries, Li–S batteries show a higher theoretical specific capacity (1672 mA h g^{-1}) and high energy density (2600 W h kg^{-1}) thus showing a great promise to power various electric vehicles (EVs) and portable electronic devices.[1] Moreover, a rather low price, high abundance and nontoxicity of sulfur active material also makes Li–S batteries more attractive. Nevertheless, so far, Li–S batteries still suffer from apparent inherent limitations, which have seriously hampered their real applications. For example, at room temperature, poor electronic conductivity (5×10^{-30} S cm^{-1}) positively causes poor electrochemical accessibility and low active material utilization. In addition, large sulfur volumetric expansion (~80%) during the lithiation process usually results in a deteriorated cycling performance. Much worse, the dissolution of long-chain lithium polysulfide intermediates Li_2S_n ($4 \leq n \leq 8$) and their "shuttle effect" in organic liquid electrolytes lead to active material loss, poor cycling stability and low coulombic efficiency of Li–S batteries.[2]

The universal solution for such issues is combining sulfur with carbonaceous materials, such as porous hollow carbon spheres,[3–8] carbon nanotubes,[9–12] graphene[13,14] and 3D porous carbon aerogels,[15] which could enhance the electron transfer and hinder the polysulfide diffusion, allowing high stability of the sulfur cathodes. However, the C/S cathodes still endure a capacity fading over medium-term cycling, because the nonpolar carbon can only provide a weak interaction to anchor a polar LiPS species. Recently, many studies have demonstrated that a chemically-modified carbon framework by heteroatom doping (such as N, S and B) can immobilize LiPS *via* chemical binding to some extent. Interestingly, when compared with undoped and single N-doped carbons, S- and S, N co-doped carbons have shown stronger LiPS chemisorption.[16–19] The quantum chemistry calculations also indicate that pyridinic N/adjacent thionic S functionalities synergistically bind small Li_2S/Li_2S_2 molecules, which mainly contributes to the improved performance.[16]

As the newly-emerged porous materials, metal–organic frameworks (MOFs) possess periodically porous structures and chemical compositions, offering the chance to convert them

[a]State Key Lab of Fine Chemicals, Liaoning Key Lab for Energy Materials and Chemical Engineering, PSU-DUT Joint Center for Energy Research, School of Chemical Engineering, Dalian University of Technology, Dalian 116024, China. E-mail: zbzhao@dlut.edu.cn; jqiu@dlut.edu.cn

[b]Dalian National Laboratory for Clean Energy, Dalian Institute of Chemical Physics, Chinese Academy of Sciences, 457 Zhongshan Road, Dalian 116023, China

[c]School of Chemistry, Dalian University of Technology, Dalian 116024, China

† Electronic supplementary information (ESI) available. See DOI: 10.1039/c8ta00529j

into carbon- or metal-based nanostructured materials.[20] Such porous carbons possess the following advantages: (i) hierarchical porous structures with abundant interior mesopores and large volume for loading sulfur species as well as the unique surface micropores for the physical confinement of LiPS; (ii) interconnected conductive networks for an improved sulfur utilization and lower inner resistance.[21] When compared with heteroatom-doped porous carbons, some materials with unique polar functional groups such as metal oxides (MnO_2,[22–24] TiO_2,[25] Ti_4O_7,[26,27] TiO,[28,29] ZrO_2,[30] and $Mg_{0.8}Cu_{0.2}O$[31]), polymers (polypyrrole,[32] polyaniline,[33,34] and PEDOT[35]), transition-metal disulfides (TiS_2,[36] WS_2,[37,38] Co_9S_8,[39] and Co_3S_4 (ref. 40)), metal-carbides (MXene phases),[41,42] and MOFs[43] show much stronger binding with polysulfides but inferior electronic conductivity. Most recently, graphitic carbon nitride (g-C_3N_4) has been identified as a new concept for chemically confined LiPSs in Li–S batteries, suggesting an enhanced cycling performance. The intrinsic high charge polarity of g-C_3N_4 endows enriched LiPS binding sites (pyridinic N) as demonstrated by first-principles calculations.[44] So far, there are only few reports on embedding nanosized g-C_3N_4 in porous carbon for high-performance Li–S batteries. Therefore, combining doped porous carbons with high-adsorption g-C_3N_4 can be an effective strategy to boost Li–S battery performance.

Herein, *via* a double-solvent strategy, we have successfully embedded g-C_3N_4 nanodots into a MOF-derived N, S co-doped hollow porous carbon shell (CN@NSHPC). The pores of NH_2-MIL-101(Al) play a crucial role in retarding the growth of g-C_3N_4 nanodots through the pore confinement effect. Lithium polysulfide adsorption tests indicate a remarkably strong adsorption of the CN@NSHPC composites when compared with that of the single g-C_3N_4 and doped porous carbon shells, suggesting a synergistically boosted polysulfide adsorption. After loading sulfur, the as-obtained S/CN@NSHPC composites are employed in Li–S batteries and exhibit a high coulombic efficiency, good rate capability in addition to outstanding cycling stability. The excellent battery performance can be ascribed to our rational material design, which simultaneously endows S/CN@NSHPC with high sulfur content, enhanced conductivity, and polysulfide binding.

2.1 Synthesis of NH_2-MIL-101(Al)

NH_2-MIL-101(Al) was synthesized using the reported method with modified procedures.[45] 2-Aminoterephthalic acid (2.077g, 11.5 mmol) was dissolved in *N*,*N*-dimethylformamide (DMF, 500 mL) and heated to 110 °C in an oil bath. Then, $AlCl_3 \cdot 6H_2O$ (5.53 g, 23 mmol) was added in seven equal portions with a time interval of 15 min between two additions. After the last portion was added, the reaction was kept at 110 °C for 3 h under stirring and left for an additional 16 h without stirring. After cooling to room temperature, a faint yellow solid was obtained and separated by centrifugation at 9000 rpm for 5 min; it was then washed with ethanol and DMF, finally purified in ethanol at 90 °C overnight and dried at 120 °C.

2.2 Encapsulation of ammonium thiocyanate into NH_2-MIL-101(Al)

The encapsulation of ammonium thiocyanate (AT) into the pores of NH

here, C_0 is the molar concentration of Li_2S_6 solution before adsorption; C_r is the molar concentration of Li_2S_6 solution after adsorption; V is the volume of the Li_2S_6 solution used in the adsorption test; M is the molar mass of Li_2S_6; m is the mass of the adsorbent. The adsorption capacities of Li_2S_6 on g-C_3N_4, NPC, CN@NSHPC/Al_5O_6N and CN@NSHPC were about 0.10, 1.90, 1.83 and 2.02 g g^{-1}, respectively.

2.6 Material characterization

The morphologies of products were characterized by HR-TEM (Tecnal G2 20), TGA (DTG-60AH), XRD (Rigaku D/MAX-2400 equipped with a rotating anode and a CuKα radiation source ($\lambda = 0.15418$ nm)), XPS (Thermo ESCALAB 250Xi equipped with a monochromatic Al Kα source of 1486.5 eV), elemental analysis (Vario EL III), and UV-vis spectroscopy (lambda-750 UV-vis spectrometer).

2.7 Electrochemical measurements

The tests with Li–S battery were conducted using the CR2016 coin cells with lithium foil as the counter and reference electrodes. The galvanostatic charge/discharge tests were performed using the LAND CT2001A battery system. Cyclic voltammetry studies were carried out on the VMP-300 electrochemical workstation at a scan rate of 0.1 mV s^{-1}. For the samples, a slurry was prepared by mixing 70% active electrode material, 20% acetylene black, and 10% polyvinylidene fluoride (PVDF) binder. Then, the working electrodes were fabricated by slurry-casting on an Al foil. The electrolyte used was 1.0 M Libis(trifluoromethanesulphonyl)imide in 1,3-dioxolane and 1,2-dimethoxyethane (1 : 1 by volume) with 1.0 wt% $LiNO_3$ additive; the amount of electrolyte in a single cell was 30 μL. The Li–S batteries consisted of a prepared electrode and polypropylene separator as well as a lithium foil as the counter electrode. The average sulfur mass loading of S/CN@NSHPC was 1.7–2 mg cm^{-2}.

The synthetic strategy of fabrication of CN@NSHPC is schematically illustrated in Scheme 1. Uniform nanoparticles of NH_2-MIL-101(Al) were fabricated by coordinating-Al^{3+} with 2-aminoterephthalic acid in DMF. The XRD patterns and transmission electron microscopy (TEM) images of NH_2-MIL-101(Al) are shown in Fig. S1 and S2a,† respectively. As shown in Fig. S3a,† NH_2-MIL-101(Al) was found to possess both 1.2 nm pentagonal windows and 1.6 nm hexagonal windows.[44] Subsequently, ammoniumthiocyanate (AT) was injected into the pores of NH_2-MIL-101(Al) by a double-solvent approach (DSA) based on the wettability difference between the inner (hydrophilic) and external (hydrophobic) surfaces of such pores (Fig. S3†). Hydrophilic droplets of AT aqueous solution added to the hydrophobic *n*-hexane permeated uniformly into the inner pores of NH_2-MIL-101(Al) (Fig. S4†). The aqueous AT guests could be enclosed into the hydrophilic pores by the capillary action and hydrophilic groups. Eventually, CN@NSHPC was obtained by annealing the intermediates at 600 °C in an Ar atmosphere. Interestingly, during the formation of g-C_3N_4, AT decomposed and released a large amount of H_2S and NH_3 (Fig. S5†), which could etch the interior of NH_2-MIL-101(Al), resulting in a unique hollow N, S co-doped carbon framework.

The variation in morphology of the materials during the synthesis process was examined by TEM. Fig. 1a shows that AT@NH_2-MIL-101(Al) had a typical solid spheroidal nanoparticle morphology with well-kept structural features of the NH_2-MIL-101(Al) template (Fig. S2a†). After annealing and acid-etching to remove metal particles, the TEM images of as-obtained CN@NSHPC demonstrated a unique hollow structure (Fig. 1c). The high-resolution transmission electron microscopy (HR-TEM) result further suggested that the g-C_3N_4 nanodots had been embedded into the hollow carbon shells with a thickness of *ca.* 30 nm and displayed a lattice spacing of 0.330 nm, which was ascribed to the (002) plane of g-C_3N_4, suggesting the presence of g-C_3N_4 nanodots with a size less than 5 nm. This result indicated the confinement effect of the pores in NH_2-MIL-101(Al) on inhibiting the (self-aggregation and growth) of g-C_3N_4 (Fig. 1d and S3†).[46,47] For comparison, bare NH_2-MIL-101(Al) was also directly pyrolyzed, resulting in NPC with a size of about 150 nm (Fig. 1b). The energy-dispersive spectrometry (EDS) elemental mapping obtained from TEM image shown in Fig. 1e and f exhibited well-corresponded C, N,

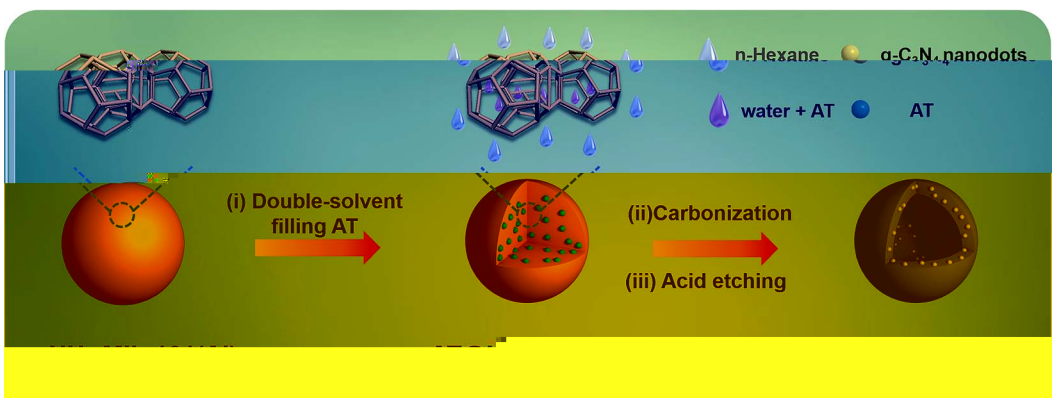

Schematic illustration of the procedure for fabricating CN@NSHPC.

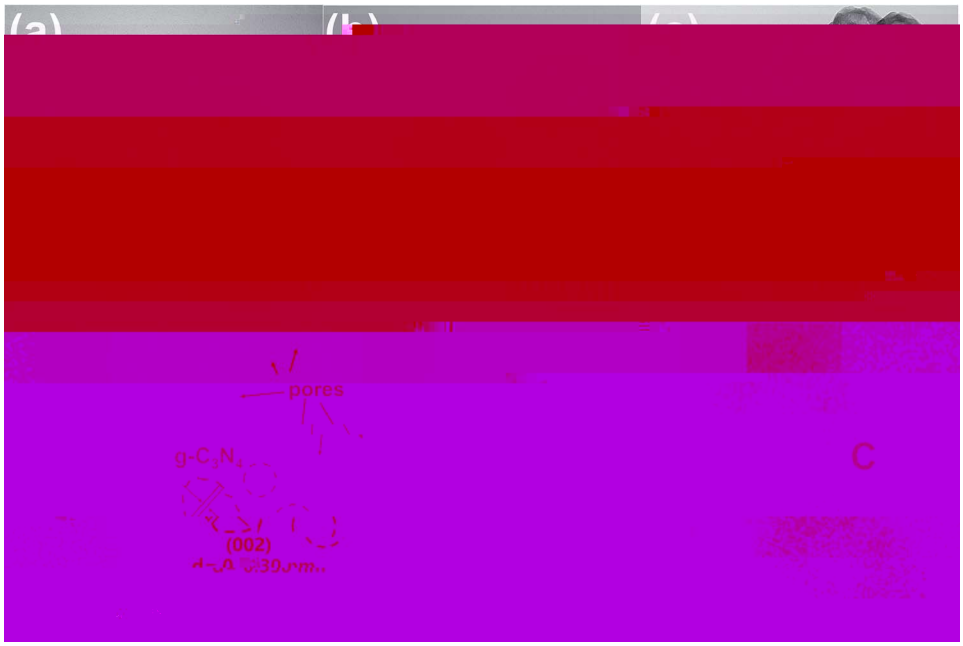

. . TEM images of (a) AT@NH_2-MIL-101(Al), (b) NPC and (c) CN-5@NSHPC. (d) HR-TEM image of CN-5@NSHPC. (e and f) TEM image and elemental mapping of CN-5@NSHPC.

O, and S element distributions, suggesting a uniform doping of these elements in CN@NSHPC. Such results demonstrated the reasonability of employing AT as a single g-C_3N_4 precursor (Fig. S2b†) for the fabrication of homogeneously N, S co-doped carbon hollow structures.

Fig. 2a shows the FT-IR spectra of CN@NSHPC, NPC and g-C_3N_4. The absorption peaks of CN@NSHPC at about 1645 and 1384 cm^{-1} are attributed to C–N heterocycle stretching modes. The peak at 808 cm^{-1} stems from the characteristic breathing of the triazine units.[48] When compared with g-C_3N_4, NPC and CN@NSHPC display the weakened featured peaks of the triazine units at 808 cm^{-1}, which can be derived from the nanosized embedding effect. This result is in agreement with the results from a previous report.[47] Powder X-ray diffraction (XRD) patterns of g-C_3N_4, NPC, CN@NSHPC and CN-5@NSHPC/Al_5O_6N are shown in Fig. 2b and S6.† The XRD pattern of g-C_3N_4 is well-corresponded with the result reported elsewhere on g-C_3N_4 synthesized by polymerization of ammoniumthiocyanate.[48] The peak at 27° and 13° corresponding to the calculated interlayer of d = 0.33 nm and 0.675 nm can be indexed to the (002) and (100) peaks of the characteristic stacking of conjugated aromatic systems and in-planar ordering of the tri-*s*-triazine units, respectively. The broad peak between 20° and 30° observed in NPC is ascribed to the (002) peak of amorphous carbon. Interestingly, both CN-5@NSHPC and CN-5@NSHPC/Al_5O_6N display a diffraction peak at 26.3° with an interlayer distance of 0.339 nm, which may be attributed to the composite structure of the inseparable combination of NPC and g-C_3N_4 nanodots through the covalent interactions. This is the reason why CN-5@NSHPC and CN-5@NSHPC/Al_5O_6N show diffraction patterns that are different from those of g-C_3N_4 and NPC. In addition, three weak peaks from metallic Al_5O_6N can be observed in the XRD pattern of CN-5@NSHPC/Al_5O_6N before etching with HF solution.[52] During the annealing process, Al_5O_6N is formed around the scaffold of carbon skeleton by the reaction between NH_2-MIL-101(Al) and NH_3 released during the pyrolysis of AT.

Raman spectroscopy is further used to characterize the disorder in the sp^2 carbon materials. The D-band of CN-5@NSHPC shifts from 1354 to 1348 cm^{-1} and the G-band clearly shifts from 1578 to 1582 cm^{-1} when compared with those of NPC, which is caused by the covalent interactions of g-C_3N_4 nanodots and is similar to the results in a previous

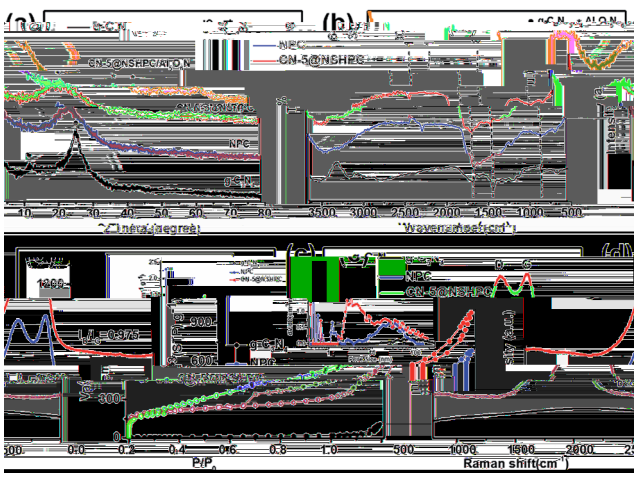

. . (a) FT-IR spectra of g-C_3N_4, NPC and CN-5@NSHPC. (b) XRD patterns of g-C_3N_4, NPC, CN-5@NSHPC and CN-5@NSHPC/Al_5O_6N. (c) Raman spectra and (d) N_2 sorption isotherms at 77 K (the inset shows pore size distributions) of g-C_3N_4, NPC and CN-5@NSHPC.

report.[52] Moreover, the ratio of D- to G-band intensity of CN-5@NSHPC is 0.975, significantly larger than that of NPC (0.940), which implies much more defects in the CN-5@NSHPC carbon shell (Fig. 2c and Table S3†). The N_2 adsorption–desorption isotherms of NPC and CN-5@NSHPC are type IV profiles (Fig. 2, S7 and Table S1†), indicating the presence of mesopores and micropores in these two samples. The BET surface areas of g-C_3N_4, NPC and CN-5@NSHPC are 25, 772 and 972 $m^2\ g^{-1}$, respectively, whereas the pore size distributions are determined by the QS-DFT model, and the results consist of three peaks located at 23, 6.1 and 6.0 nm for these materials. When compared with the bigger microporous structure of g-C_3N_4, the structures of NPC and CN-5@NSHPC possess smaller micro- and mesopores. The porous structure shows that the increase of surface area can be due to the etching effect of NH_3 and H_2S on the MOF skeleton, which contributes to an extra hollow space for the carbon materials.[53] Besides, specific surface area of CN-9@NSHPC is 518 $m^2\ g^{-1}$, indicating that g-C_3N_4 generated in excess can reduce the specific surface area.

The chemical composition of the obtained materials is investigated by X-ray photoelectron spectroscopy (XPS), revealing the presence of C, O, N and S (Fig. 3a–e). The N contents of CN-5@NSHPC and g-C_3N_4 are 13.3% and 47.2%, respectively. The XPS spectra of C 1s with different contents of AT and g-C_3N_4 (Fig. 3a) exhibit two similar peaks; when compared with pure g-C_3N_4, all of the CN@NSHPC samples demonstrate a slight shift of binding energy from 287.7 eV to 288.2 eV. This shift can be attributed to the interactions between the g-C_3N_4 nanodots and carbon matrix,[46] which benefit the retention of the composite structure during the charge and discharge processes in the operation of lithium–sulfur battery.[54] In addition, in the high-resolution N 1s spectra (Fig. 3c, S8 and Table S2†), both CN@NSHPC and g-C_3N_4 display components corresponding to an sp^2-bonded N involved in the triazine rings (C–N=C) at 398.7 eV, tertiary nitrogen N–$(C)_3$ group (400.2 eV) and secondary amine (C–N–H_2) at 401.8 eV. Other reports confirm that C–N–H_2 plays a role in the covalent link between carbon and g-C_3N_4 nanodots.[49] Moreover, as shown in Fig. 3d, the S 2p spectrum can be deconvoluted into three peaks at 164.7 eV, 163.3 eV, and 168.6 eV associated with three classified sulfur species. The previous two peaks are attributed to the spin–orbit coupling of the electrons in the p-orbital, and the peak at 168.6 eV is assigned to oxidized sulfur species. The S content of CN-5@NSHPC is 3.7%. However, there is no clear signal attributed to the S 2p found in g-C_3N_4 synthesized from AT (Fig. 3e), which is similar to the results in a previous report.[50,51] g-C_3N_4@N, S co-doped in hollow porous carbon is crucial to chemically absorb soluble LiPS species as determined by the LiPS adsorption experiments (Fig. 5).

Coin cells with Li foil as an anode and the as-prepared S/CN-5@NSHPC (Fig. S9a†) composite as the cathode were fabricated to evaluate the electrochemical performance of the materials. In the first cathodic scan of cyclic voltammetry curves, there were two well-defined reduction peaks at 2.04 V and 2.31 V, implying that the processes of S_8 to long-chain lithium polysulfides (Li_2S_n, $4 \leq n \leq 8$) and long-chain lithium polysulfides to the lower polysulfides (Li_2S_n, $n \leq 2$), respectively, occurred. The oxidation process of the cathode also occurred at two stages. The first oxidation peak at 2.41 V was associated with the formation of Li_2S_n ($n > 2$), which was oxidized to S_8 at 2.51 V. The second oxidation peak at around 2.51 V was more distinct than that of the ever-reported results;[55] this indicated the more complete oxidation of high-order Li_2S_n to S_8 on the surface of the CN-5@NSHPC composite, which was attributed to the effective adsorption of Li_2S_n on the g-C_3N_4 surface and the effective transformation of Li_2S_n to S_8.[56] The representative galvanostatic charge–discharge profiles of the S/CN-5@NSHPC cathode between 1.5 V and 3.0 V at 1C are shown in Fig. 4b. The S/CN-5@NSHPC cathode exhibited two discharging

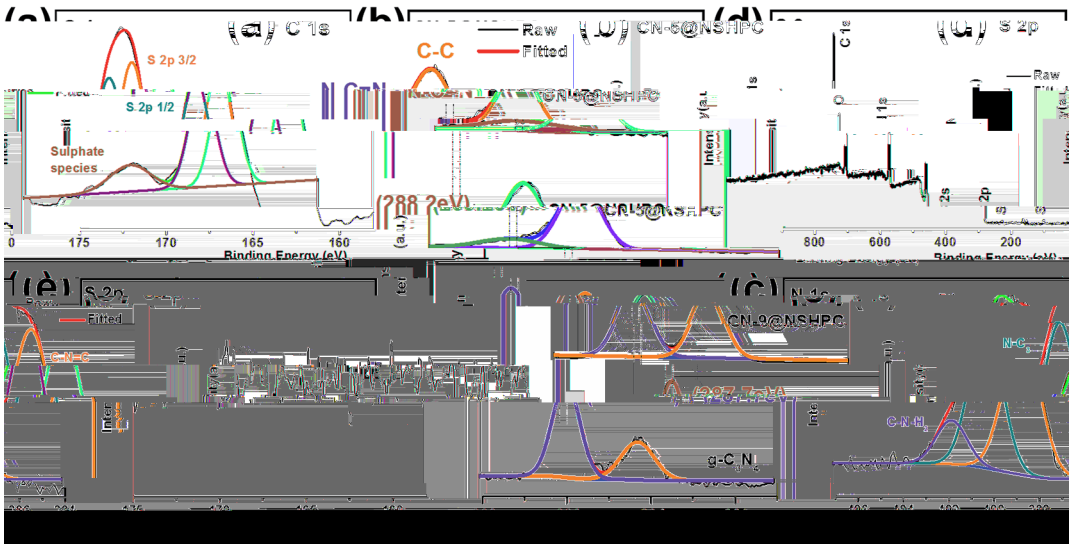

(a) High-resolution C 1s XPS spectra of CN@NSHPC and g-C_3N_4. (b–d) XPS survey spectra of CN-5@NSHPC and high-resolution XPS spectra of N 1s and S 2p. (e) XPS spectrum of g-C_3N_4: the S 2p region.

plateaus and a charging plateau, which was consistent with the results of CV curves. Furthermore, the electrochemical impedance spectroscopy (EIS) measurements of S/CN-5@NSHPC, S/NPC, S/g-C_3N_4, S/CN-3@NSHPC and S/CN-9@NSHPC were studied to explore their electrochemical dynamics in freshly assembled batteries. The spectra were fitted using an equivalent circuit shown in the inset of Fig. 4c and 6c, in which R_s represents the ohmic resistance including electron and ion conductivity, R_{ct} is the charge-transfer resistance of the electrochemical reaction, and CPE arises from the double-layer capacitance. Impressively, R_{ct} of S/CN-5@NSHPC was lower than those of S/NPC, S/g-C_3N_4, S/CN-3@NSHPC and S/CN-9@NSHPC, indicating that the CN@NSHPC composite structures offered faster ion diffusion and higher electrical conductivity.[57]

Fig. 4d shows the rate capability of S/CN-5@NSHPC at different current densities. The average discharge specific capacity was 1447 mA h g^{-1} at 0.2C. When the current rates increased to 0.5, 1, 2, 3, 4 and 5C, the electrode exhibited reversible capacities of 1072, 739, 583, 488, 456 and 387 mA h g^{-1}, respectively. When the current density was switched from 5C back to 0.2C, S/CN-5@NSHPC still exhibited a high capacity of 1005 mA h g^{-1}. When compared with the S/

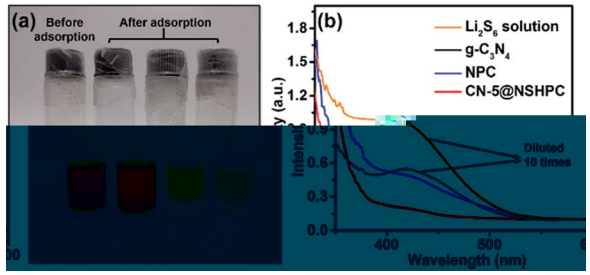

(a and b) a digital photograph and UV-vis absorption results of the Li_2S_6 solution before and after the addition of g-C_3N_4, NPC and CN-5@NSHPC.

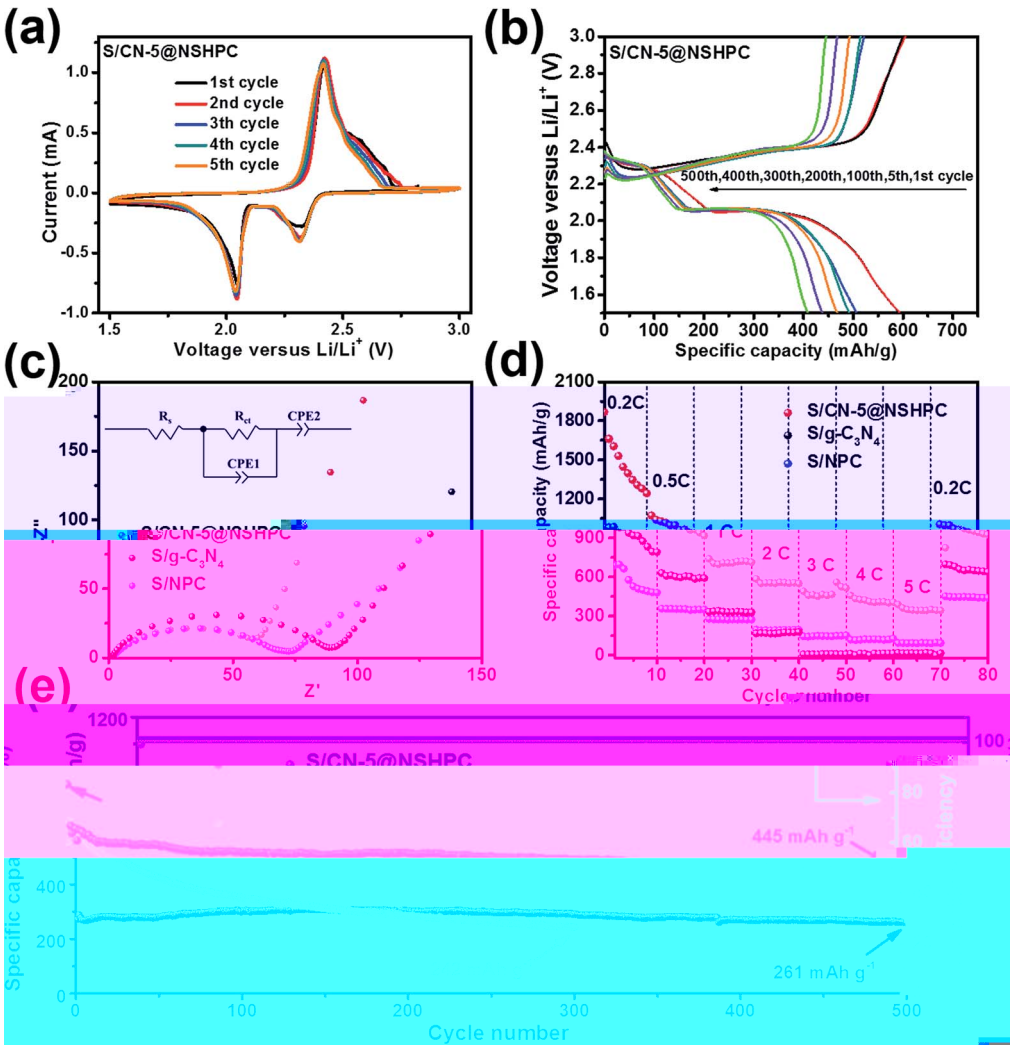

(a) Cyclic voltammograms (CV) of S/CN-5@NSHPC obtained at a scan rate of 0.1 mV s^{-1} between 1.5 and 3.0 V. (b) Charge and discharge voltage profiles of S/CN-5@NSHPC. (c) EIS plots of S/CN-5@NSHPC, S/NPC and S/g-C_3N_4 (the inset is the equivalent circuit used). (d) Rate capabilities of S/CN-5@NSHPC, S/NPC and S/g-C_3N_4 tested at various current densities ranging from 0.2C to 5C. (e) Cycling performances of S/CN-5@NSHPC, S/NPC and S/g-C_3N_4 tested at a current density of 1C.

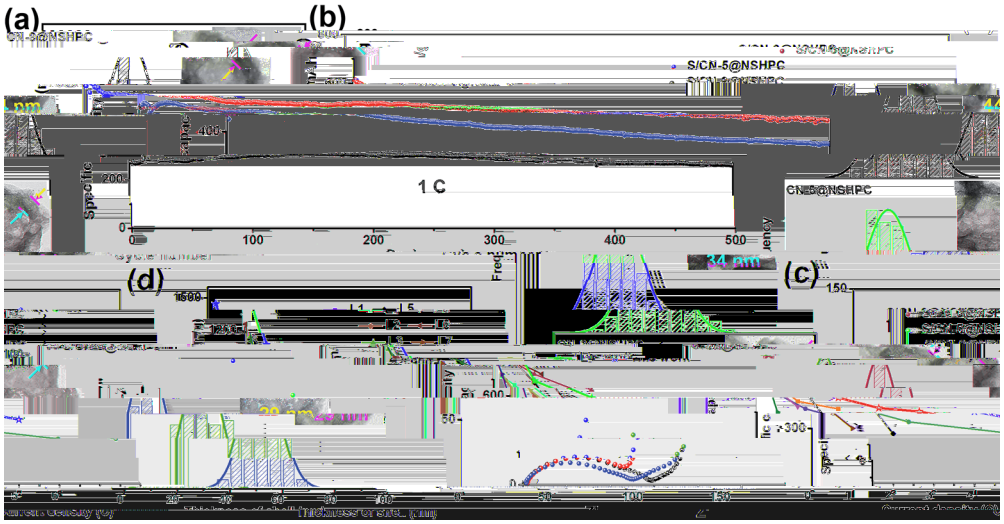

(a) Shell thickness distribution histogram of CN@NSHPC. (b) Comparative cycling performance of S/CN-3@NSHPC, S/CN-5@NSHPC and S/CN-9@NSHPC. (c) EIS plots of the S/CN-3@NSHPC, S/CN-5@NSHPC and S/CN-9@NSHPC cathodes. (d) Comparisons of specific capacities of S/CN-5@NSHPC with hollow porous carbon for lithium–sulfur battery at different rates with the materials reported in the literature (L1: N-doped hollow porous carbon microspheres, L2: yolk–shell carbon microspheres, L3: ultrahigh-surface-area hollow carbon nanospheres, L4: double-shelled nanocages, L5: N-doped hollow carbon nanospheres, L6: hollow-in-hollow carbon spheres, L7: double-shelled hollow carbon spheres, this study: g-C_3N_4@ N, S co-doped hollow porous carbon).

NPC and S/g-C_3N_4 cathodes, the S/CN-5@NSHPC cathode showed overwhelming superiority on the rate capability at the same rates.

The long-term cycling stabilities of S/CN-5@NSHPC, S/NPC and S/g-C_3N_4 were further investigated at 1C (Fig. 4e). When compared with S/NPC and S/g-C_3N_4 cathodes, the S/CN-5@NSHPC cathode showed a better electrochemical performance, specifically, a capacity of 1099 mA h g^{-1} in the initial discharge process. After 2 cycles of activation at 0.1C, the reversible capacity of S/CN-5@NSHPC was 615 mA h g^{-1}. When cycled at 1C over 500 cycles, the reversible capacity of S/CN-5@NSHPC remained at 445 mA h g^{-1}, corresponding to 72.3% capacity retention, indicating an ultralow capacity decay of 0.048% per cycle. Interestingly, there was no evident structural damage of the electrode as was observed in the TEM results (Fig. S10†). Additionally, the excellent coulombic efficiency of S/CN-5@NSHPC was also obtained, typically, 95% over 500 cycles. By contrast, S/NPC and S/g-C_3N_4 displayed low initial discharge capacities of 535 and 273 mA h g^{-1}, which quickly dropped to 242 and 290 mA h g^{-1}, respectively, after 300 cycles. The obvious capacity loss of the controlled materials could be attributed to the diffusion and solvation of LiPS in the electrolyte.[58]

The polysulfides (Li_2S_6)–tetrahydrofuran solution absorptivity tests of the cathode materials were conducted for quantitative detection. As shown in Fig. 5a, after the adsorption by g-C_3N_4 and NPC, the color of the Li_2S_6 solution changed from an original deep orange to orange and canary yellow, respectively. By contrast, the solution color became clearly transparent after the addition of CN-5@NSHPC, suggesting an excellent absorption capability of this material. Moreover, the UV-vis spectra demonstrated that CN-5@NSHPC could adsorb polysulfide roughly dozen times as much as g-C_3N_4 (Fig. 5b and S11†). The high superior rate and stable cycling performance of the CN@NSHPC cathode could be ascribed to the following reasons: (i) the g-C_3N_4 nanodots, which resulted from the pore confinement effect and were evenly dispersed in the hollow carbon shell, could improve the utilization of the active material and shorten the transport paths for ions/electrons. As a result, the cycling stability and rate capability of the electrodes improved.[59–61] (ii) the outstanding polysulfide adsorption ability of CN@NSHPC benefitted from the synergistic effect of N, S co-doped, nanosized g-C_3N_4 embedding and hollow porous structure design, which was in agreement with the results of the reported literature.[16,17,54,62]

The effect of AT content on the structures and electrochemical properties of CN@NSHPC has been investigated. As shown in Fig. 6a, the shell thickness increases with an increase in AT (Fig. 6a and S12†). Fig. S15 and Table S1† illustrate the surface area and pore size distribution of CN@NSHPC. Obviously, the CN@NSHPC materials are composed of enriched micropores and mesopores, and the thermal decomposition of AT enables the modification of the surface area and porous structure of NH_2-MIL-101(Al). The surface areas of S/CN-3@NSHPC, S/CN-5@NSHPC and S/CN-9@NSHPC are 702, 972 and 518 m^2 g^{-1}, respectively. Raman spectra of CN@NSHPC are shown in Fig. S13.† The ratio of D- (1346 cm^{-1}) to G-band (1558 cm^{-1}) intensity implies that an increasing amount of AT etches the carbon and results in the formation of more defect sites outside the carbon shell (Table S3†). S/CN-5@NSHPC shows a very stable cycling performance that outputs a specific capacity of 445 mA h g^{-1} at the 500th cycle with a current density of 1C. At the same time, the capacities of S/CN-3@NSHPC and S/CN-9@NSHPC under the same

conditions decrease to 348 mA h g^{-1} and 261 mA h g^{-1}, respectively (Fig. 6b). Obviously, S/CN-5@NSHPC with a moderate loading of AT shows the highest cycling performance among these materials (Fig. S14†). This result indicates that inadequate g-C_3N_4 nanodots of S/CN-3@NSHPC cannot form a strong interaction to anchor polar LiPS species, bringing about slightly higher cyclic stability than that of S/NPC. In addition, S/CN-9@NSHPC has excess g-C_3N_4 nanodots, which may block a part of the micropores and mesopores (Fig. S15†) and thicken the shell of the hollow porous carbons, causing poor electron and lithium-ion transportation and low S utilization.[6,70,71] With a suitable loading of g-C_3N_4 nanodots, the LiPS dissolution has been effectively restrained. In addition, the LiPS dissolution can be effectively prohibited under this condition. The rate capability of S/CN-5@NSHPC obtained in the present study is compared with some results on carbon materials having hollow porous structures previously reported in the literature (Fig. 6d).

Conclusions

In summary, we have rationally developed novel *in situ* N, S co-doped hollow porous carbons embedded with nanosized g-C_3N_4 *via* a facile double-solvent approach coupled with controllable AT@NH_2-MIL-101(Al) pyrolysis. The unique hollow nanostructures are created *via* the gases released during AT decomposition, and g-C_3N_4 nanodots having sizes less than 5 nm are formed simultaneously based on the pore confinement effect. The nanosized g-C_3N_4 embedded in the N, S co-doped porous carbon shells endows CN@NSHPC with a high sulfur loading and LiPS adsorption capacity as well as an enhanced electrical conductivity. When applied as a cathode in lithium–sulfur batteries, the as-created materials exhibit an ultralow capacity decay of 0.048% over 500 cycles at 1C. The excellent performance can be attributed to the synergistic effect of hollow design of carbon shells, N, S co-doping, and nanosized g-C_3N_4 embedding, which effectively facilitate the electron transfer and inhibit the shuttle effect of polysulfides. This proposed strategy can enlighten the construction of hollow nanostructured and nanosized materials for other electrochemical applications such as in lithium-ion batteries and supercapacitors.

Conflicts of interest

There are no conflicts to declare.

Acknowledgements

This study is supported by the National Natural Science Foundation of China (Grant No. U1610105, 51672033, and U1610255), the Natural Science Foundation of Liaoning Province (201602170), the Open Fund of Key Laboratory of Interface Science and Engineering in Advanced Materials, Ministry of Education (KLISEAM 201601), and the Open Sharing Fund Projects for Large Equipments Testing, Dalian University of Technology (2016-54).

References

1 P. G. Bruce, S. A. Freunberger, L. J. Hardwick and J. M. Tarascon, *Nat. Mater.*, 2011, **11**, 119–129.
2 X. Ji, K. T. Lee and L. F. Nazar, *Nat. Mater.*, 2009, **8**, 500–506.
3 N. Jayaprakash, J. Shen, S. S. Moganty, A. Corona and L. A. Archer, *Angew. Chem., Int. Ed.*, 2011, **50**, 5904–5908.
4 X. Wang, G. Li, J. Li, Y. Zhang, A. Wook, A. Yu, *et al.*, *Energy Environ. Sci.*, 2016, **9**, 2533–2538.
5 K. Wang, L. Huang, S. Razzaque, S. Jin and B. Tan, *Small*, 2016, **12**, 3134–3142.
6 Q. Sun, B. He, X. Q. Zhang and A. H. Lu, *ACS Nano*, 2015, **9**, 8504–8513.
7 W. Xue, Q.-B. Yan, G. Xu, L. Suo, Y. Chen, C. Wang, *et al.*, *Nano Energy*, 2017, **38**, 12–18.
8 Z. Li, B. Y. Guan, J. Zhang and X. W. Lou, *Joule*, 2017, **1**, 576–587.
9 M. Q. Zhao, H. J. Peng, G. L. Tian, Q. Zhang, J. Q. Huang, X. B. Cheng, *et al.*, *Adv. Mater.*, 2014, **26**, 7051–7058.
10 F. Jin, S. Xiao, L. Lu and Y. Wang, *Nano Lett.*, 2016, **16**, 440–447.
11 X.-B. Cheng, J.-Q. Huang, Q. Zhang, H.-J. Peng, M.-Q. Zhao and F. Wei, *Nano Energy*, 2014, **4**, 65–72.
12 M. Zhang, C. Yu, C. Zhao, *et al.*, *Energy Storage Maters*, 2016, **5**, 223–229.
13 J. Song, Z. Yu, M. L. Gordin and D. Wang, *Nano Lett.*, 2016, **16**, 864–870.
14 P. Y. Zhai, H. J. Peng, X. B. Cheng, *et al.*, *Energy Storage Maters*, 2017, **7**, 56–63.
15 G. Hu, C. Xu, Z. Sun, S. Wang, H. M. Cheng, F. Li, *et al.*, *Adv. Mater.*, 2016, **28**, 1603–1609.
16 J. Balach, H. K. Singh, S. Gomoll, T. Jaumann, M. Klose, S. Oswald, *et al.*, *ACS Appl. Mater. Interfaces*, 2016, **8**, 14586–14595.
17 Q. Pang, J. Tang, H. Huang, X. Liang, C. Hart, K. C. Tam, *et al.*, *Adv. Mater.*, 2015, **27**, 6021–6028.
18 J. Yang, F. Chen, C. Li and X. Zhou, *J. Mater. Chem. A*, 2016, **4**, 14324–14333.
19 F. Nitze, K. Fossum, S. Xiong, A. Matic and A. E. C. Palmqvist, *J. Power Sources*, 2016, **317**, 112–119.
20 W. Xia, A. Mahmood, R. Zou and Q. Xu, *Energy Environ. Sci.*, 2015, **8**, 1837–1866.
21 X. Yang, Y. Yu, N. Yan, H. Zhang, X. Li and H. Zhang, *J. Mater. Chem. A*, 2016, **4**, 5965–5972.
22 X. Liang and L. F. Nazar, *ACS Nano*, 2016, **10**, 4192–4198.
23 Z. Li, J. Zhang and X. W. Lou, *Angew. Chem., Int. Ed.*, 2015, **54**, 12886–12890.
24 S. Rehman, T. Tang, Z. Ali, X. Huang and Y. Hou, *Small*, 2017, **13**, 170087.
25 Z. Wei Seh, W. Li, J. J. Cha, G. Zheng, Y. Yang, M. T. McDowell, *et al.*, *Nat. Commun.*, 2013, **4**, 1331.
26 X. Tao, J. Wang, Z. Ying, Q. Cai, G. Zheng, Y. Gan, *et al.*, *Nano Lett.*, 2014, **14**, 5288–5294.
27 H. Wei, E. F. Rodriguez, A. S. Best, A. F. Hollenkamp, D. Chen and R. A. Caruso, *Adv. Energy Mater.*, 2017, **7**, 1601616.

28 Z. Li, J. Zhang, B. Guan, D. Wang, L. M. Liu and X. W. Lou, *Nat. Commun.*, 2016, **7**, 13065.
29 Z. Li, H. B. Wu and X. W. Lou, *Energy Environ. Sci.*, 2016, **9**, 3061–3070.
30 Y. Zhou, C. Zhou, Q. Li, C. Yan, B. Han, K. Xia, *et al.*, *Adv. Mater.*, 2015, **27**, 3774–3781.
31 Y. Zhang, X. Wu, H. Feng, L. Wang, A. Zhang, T. Xia, *et al.*, *Int. J. Hydrogen Energy*, 2009, **34**(3), 1556–1559.
32 Y. Dong, S. Liu, Z. Wang, Y. Liu, Z. Zhao and J. Qiu, *Nanoscale*, 2015, **7**, 7569–7573.
33 G.-C. Li, G.-R. Li, S.-H. Ye and X.-P. Gao, *Adv. Energy Mater.*, 2012, **2**, 1238–1245.
34 M. Wang, W. Wang, A. Wang, K. Yuan, L. Miao, X. Zhang, *et al.*, *Chem. Commun.*, 2013, **49**, 10263–10265.
35 H. Chen, W. Dong, J. Ge, C. Wang, X. Wu, W. Lu, *et al.*, *Sci. Rep.*, 2013, **3**, 1910.
36 Z. W. Seh, J. H. Yu, W. Li, P. C. Hsu, H. Wang, Y. Sun, *et al.*, *Nat. Commun.*, 2014, **5**, 5017.
37 T. Lei, W. Chen, J. Huang, C. Yan, H. Sun, C. Wang, *et al.*, *Adv. Energy Mater.*, 2016, **7**, 1601843.
38 J. Park, B.-C. Yu, J. S. Park, J. W. Choi, C. Kim, Y.-E. Sung, *et al.*, *Adv. Energy Mater.*, 2017, **7**, 1602567.
39 Q. Pang, D. Kundu and L. F. Nazar, *Mater. Horiz.*, 2016, **3**, 130–136.
40 J. Pu, Z. Shen, J. Zheng, W. Wu, C. Zhu, Q. Zhou, *et al.*, *Nano Energy*, 2017, **37**, 7–14.
41 X. Liang, A. Garsuch and L. F. Nazar, *Angew. Chem., Int. Ed.*, 2015, **54**, 3907–3911.
42 X. Liang, Y. Rangom, C. Y. Kwok, Q. Pang and L. F. Nazar, *Adv. Mater.*, 2017, **29**, 1603040.
43 J. Zhou, R. Li, X. Fan, Y. Chen, R. Han, W. Li, *et al.*, *Energy Environ. Sci.*, 2014, **7**, 2715–2724.
44 Z. Sun, J. Zhang, L. Yin, G. Hu, R. Fang, H. M. Cheng, *et al.*, *Nat. Commun.*, 2017, **8**, 14627.
45 P. Serra-Crespo, E. V. Ramos-Fernandez, J. Gascon and F. Kapteijn, *Chem. Mater.*, 2011, **23**, 2565–2572.
46 G. Li, Z. Lian, W. Wang, *et al.*, *Nano Energy*, 2016, **19**, 446–454.
47 Q. L. Zhu, J. Li and Q. Xu, *J. Am. Chem. Soc.*, 2013, **135**, 10210–10213.
48 X. Li, Y. Pi, L. Wu, Q. Xia, J. Wu, Z. Li, *et al.*, *Appl. Catal., B*, 2017, **202**, 653–663.
49 Y. Fu, J. Zhu, C. Hu, X. Wu and X. Wang, *Nanoscale*, 2014, **6**, 12555–12564.
50 Y. Cui, J. Zhang, G. Zhang, J. Huang, P. Liu, M. Antonietti, *et al.*, *J. Mater. Chem.*, 2011, **21**, 13032–13039.
51 E. S. Caballero, J. Cintas, F. G. Cuevas, J. M. Montes and M. Herrera-García, *Metall. Mater. Trans. A*, 2016, **47**, 6481–6486.
52 S. M. Unni, R. Illathvalappil, P. K. Gangadharan, S. N. Bhange and S. Kurungot, *Chem. Commun.*, 2014, **50**, 13769–13772.
53 X. Li, Q. Sun, J. Liu, B. Xiao, R. Li and X. Sun, *J. Power Sources*, 2016, **302**, 174–179.
54 Q. Pang, X. Liang, C. Y. Kwok, J. Kulisch and L. F. Nazar, *Adv. Energy Mater.*, 2016, **7**, 1601630.
55 Z. Meng, Y. Xie, T. Cai, *et al.*, *Electrochim. Acta*, 2016, **210**, 829–836.
56 Y. J. Li, J. M. Fan, M. S. Zheng, *et al.*, *Energy Environ. Sci.*, 2016, **9**, 1998–2004.
57 Z. Li, C. Li, X. Ge, J. Ma, Z. Zhang, Q. Li, *et al.*, *Nano Energy*, 2016, **23**, 15–26.
58 J. Liu, W. Li, L. Duan, X. Li, L. Ji, Z. Geng, *et al.*, *Nano Lett.*, 2015, **15**, 5137–5142.
59 Y. J. Hong, K. C. Roh and Y. C. Kang, *Carbon*, 2018, **126**, 394–403.
60 Y. An, Z. Zhang, H. Fei, *et al.*, *ACS Appl. Mater. Interfaces*, 2017, **9**, 12400–12407.